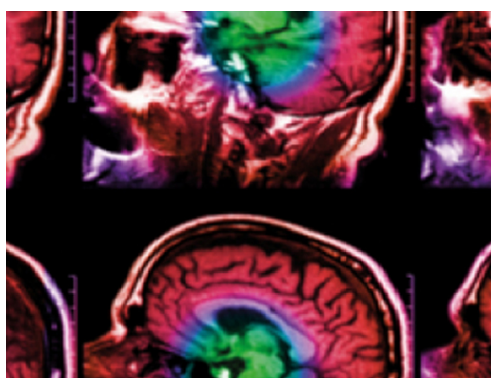


PAPER

Single spectrum three-material decomposition with grating-based x-ray phase-contrast CT

To cite this article: Eva-Maria Braig *et al* 2020 *Phys. Med. Biol.* **65** 185011

View the [article online](#) for updates and enhancements.



IPEM | IOP

Series in Physics and Engineering in Medicine and Biology

Your publishing choice in medical physics,
biomedical engineering and related subjects.

Start exploring the collection—download the
first chapter of every title for free.



PAPER

OPEN ACCESS

RECEIVED
19 February 2020REVISED
4 May 2020ACCEPTED FOR PUBLICATION
27 May 2020PUBLISHED
15 September 2020

Original Content from this work may be used under the terms of the [Creative Commons Attribution 3.0 licence](#).

Any further distribution of this work must maintain attribution to the author(s) and the title of the work, journal citation and DOI.



Single spectrum three-material decomposition with grating-based x-ray phase-contrast CT

Eva-Maria Braig¹ , Daniela Pfeiffer², Marian Willner¹, Thorsten Sellerer¹, Kirsten Taphorn^{1,2}, Christian Petrich¹, Josef Scholz¹, Lisa Petzold¹, Lorenz Birnbacher^{1,2}, Martin Dierolf¹ , Franz Pfeiffer^{1,2,3} and Julia Herzen¹

¹ Chair of Biomedical Physics, Department of Physics and Munich School of BioEngineering, Technical University of Munich, 85748 Garching, Germany

² Department of Diagnostic and Interventional Radiology, Klinikum rechts der Isar, Technical University of Munich, 81675 München, Germany

³ Institute for Advanced Study, Technical University of Munich, 85748 Garching, Germany

E-mail: eva.braig@mytum.de

Keywords: grating-based phase-contrast, material decomposition, x-ray dark-field imaging, x-ray phase-contrast imaging

Supplementary material for this article is available [online](#)

Abstract

Grating-based x-ray phase-contrast imaging provides three simultaneous image channels originating from a single image acquisition. While the phase signal provides direct access to the electron density in tomography, there is additional information on sub-resolutional structural information which is called dark-field signal in analogy to optical microscopy. The additional availability of the conventional attenuation image qualifies the method for implementation into existing diagnostic routines. The simultaneous access to the attenuation coefficient and the electron density allows for quantitative two-material discrimination as demonstrated lately for measurements at a quasi-monochromatic compact synchrotron source. Here, we investigate the transfer of the method to conventional polychromatic x-ray sources and the additional inclusion of the dark-field signal for three-material decomposition. We evaluate the future potential of grating-based x-ray phase-contrast CT for quantitative three-material discrimination for the specific case of early stroke diagnosis at conventional polychromatic x-ray sources. Compared to conventional CT, the method has the potential to discriminate coagulated blood directly from contrast agent extravasation within a single CT acquisition. Additionally, the dark-field information allows for the clear identification of hydroxyapatite clusters due to their micro-structure despite a similar attenuation as the applied contrast agent. This information on materials with sub-resolutional microstructures is considered to comprise advantages relevant for various pathologies.

1. Introduction

Computed tomography (CT) is an indispensable tool in modern diagnostic imaging in all fields from emergency care (Larson *et al* 2011) to pediatrics (Miglioretti *et al* 2013) thanks to its broad accessibility, fast image acquisition and ongoing progress in dose reduction (Kane *et al* 2008, Kim *et al* 2015, Korn *et al* 2012). Different imaging protocols concerning acceleration voltage, contrast agent application and subsequent gray value windowing allow for the diagnosis of a variety of pathologies in almost all body parts (Webb *et al* 2019). However, when it comes to materials that exhibit similar Hounsfield units (HU), a clear diagnosis is not possible (Payabvash *et al* 2014, McCollough *et al* 2015). An example for the clinical relevance of material discrimination is depicted in figure 1 for two ischemic stroke patients who underwent interventional thrombectomy. The unenhanced control scan 12 hours after the intervention shows a hyperdensity in the

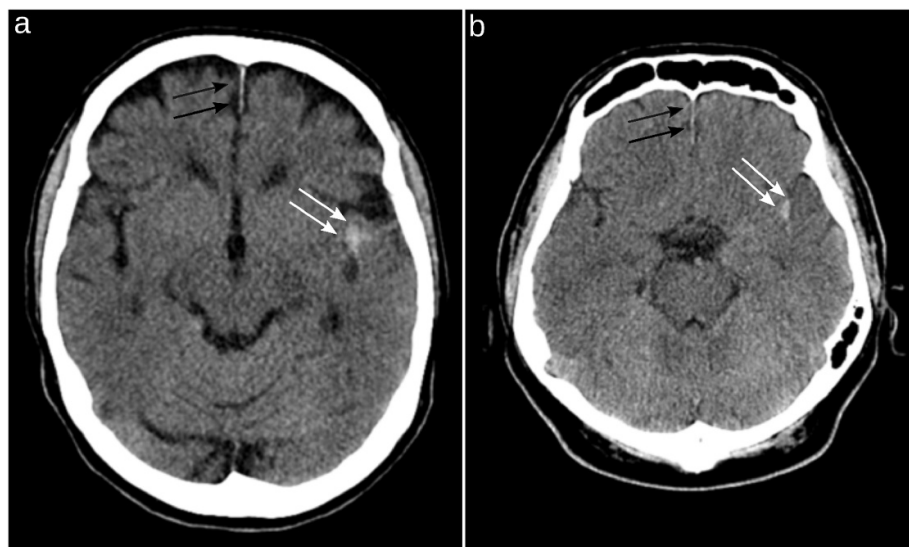


Figure 1. Unenhanced clinical CT control scans 12 hours after interventional thrombectomy. Both patients show a hyperdensity. (a) 76 year old patient with a hyperdensity in the left insular region (white arrows, 57 HU) and partially calcified falx cerebri (black arrows, 58 HU). Follow-up MRI revealed subarachnoidal bleeding. (b) 50 year old patient with a hyperdensity on the left insular region (white arrows, 55 HU) and a partial calcification of the falx cerebri (black arrows, 53 HU). Subsequent MRI showed no hemorrhage and the hyperdensity is consistent with extravasated iodine contrast agent after mechanical thrombectomy. Due to the similar attenuation coefficients, mechanically induced hemorrhage cannot be discriminated from extravasation of iodine-based contrast agent via the damaged blood brain barrier in conventional CT. Hemorrhage, contrast agent and calcifications present with nearly identical HU numbers for these patients. Retrospective analysis of patient's image data was approved and conducted in accordance with the guidelines of the institutional review board. Informed consent was waived by the institutional review board due to the retrospective design of the study.

subarachnoidal space for both patients. While follow-up magnetic resonance imaging (MRI) revealed subarachnoidal bleeding for one patient, the hyperdensity was assigned to contrast agent extravasation via the damaged blood brain barrier for the other patient. An intracerebral hemorrhage is associated with high mortality and requires an entirely different therapy than the thrombolytic prevention of further ischemic events for the other patient (Mokin *et al* 2012, Gupta *et al* 2010). Beside the discrimination of iodine contrast agent and blood, it can also be challenging to differentiate between these two materials and calcification as all three materials may present with identical attenuation values in conventional CT (see figure 1).

Dual-energy (DE) or spectral CT is able to discriminate materials with similar HU and has been implemented into the clinical practice during the last few years (Johnson *et al* 2007, Postma *et al* 2012, Graser *et al* 2009, Jacobsen *et al* 2018). The method is based on the extraction of the linear attenuation coefficient at two different energies, either with a special detector system or by using two different acceleration voltages, with the purpose of quantitative material decomposition. It has been shown that DE-CT can help to reliably differentiate hemorrhage from iodinated contrast material without employing any additional radiation and helps to initiate the right therapy, promptly (Phan *et al* 2012, Gupta *et al* 2010, Tijssen *et al* 2014, Djurdjevic *et al* 2017). Recently, we demonstrated how the same information can also be extracted from a single CT acquisition via grating-based phase-contrast CT (gbpc-CT) at a compact synchrotron source (Braig *et al* 2018). Gbpc-CT allows for the simultaneous extraction of the attenuation coefficient and the electron density within a single image acquisition (Pfeiffer *et al* 2006). It has been demonstrated that the electron density and the effective atomic number of different materials can be precisely determined with gbpc-CT at synchrotron sources as well as at conventional lab-based x-ray tube sources (Qi *et al* 2010, Herzen *et al* 2009, Willner *et al* 2013, Sarapata *et al* 2015, Birnbacher *et al* 2016, Birnbacher *et al* 2018). Further, gbpc-CT provides access to sub-resolution refractive index fluctuations (Pfeiffer *et al* 2008) as associated with tissues with a micro morphology such as the lung alveoli (Bech *et al* 2013, Schleede *et al* 2012), bone trabeculae (Potdevin *et al* 2012, Wen *et al* 2009) or microcalcifications (Michel *et al* 2013, Scherer *et al* 2016) among others.

Here, we investigate whether this threefold imaging signal can be used for three-material decomposition at conventional polychromatic x-ray sources operated with more than 40 keV mean energy. In contrast to the prior approach (Braig *et al* 2018) and especially to DE-CT, we will evaluate the use of the x-ray dark-field signal in addition to attenuation and phase contrast to simultaneously differentiate between blood coagula, contrast agent and hydroxyapatite clusters.

Table 1. Interferometer specifications. Grating periods p_i , material of the phase grating G1, lamellae heights h , inter-grating distances d and design energy E_D for the three used grating interferometers.

Setup	$p_0/p_1/p_2$	G1-material	h	d	E_D
S1	10./5./10. μm	Ni	200/8/165 μm	92.7 cm	45 keV
S2	5.4/5.4/5.4 μm	Au	65/5.2/65 μm	85.6 cm	27 keV
S3	-/4.92/5. μm	Ni	-/4.39/70 μm	24.8 cm	25 keV

2. Methods

Sample preparation

Iodine solutions were prepared by mixing powdery potassium iodide (KI) (*Sigma Aldrich, Missouri, USA*) with pure water. The respective amount of KI was determined to get an iodine concentration series of 1.0, 1.5, 2.0, 2.5 and 3.0 mg/ml. The concentrations were verified by a measurement at the Munich Compact Light Source (MuCLS), which is a quasi-monochromatic compact synchrotron source with the mean energy adjusted to 25 keV and a bandwidth of 3%. Via the measured attenuation coefficient, the concentrations were determined to be (1.1 ± 0.1) mg/ml, (1.7 ± 0.1) mg/ml, (2.2 ± 0.1) mg/ml, (3.1 ± 0.1) mg/ml and (3.6 ± 0.1) mg/ml with the statistical error derived from the standard deviation of the attenuation coefficient measurement. There was a time gap between the actual decomposition experiment and the verification measurement of seven weeks. All iodine concentrations indicated in this article refer to these measured concentrations as a ground truth.

A small amount of blood was drawn from a volunteer person (in accordance with local ethics committee decision No. 97/18 S). During the coagulation process, the blood was slightly stirred and some of the separating plasma was removed in order to get a homogeneous blood coagulum. The contrast agent solutions and the coagulated blood were poured into small plastic tubes (0.54 cm outer diameter) and mounted on a cylindrical sample holder (see 2(b)).

A small part of the frontal lobe of a pig's brain was cut to fit into a conical plastic container with 2.9 cm outer diameter. The sample was obtained from a local butchery, no animals had to be sacrificed for this study. The brain was fixated in a 4% formaldehyde solution. Additionally, a small plastic tube (0.54 cm outer diameter) filled with coagulated blood and two tubes filled with an iodine contrast agent solution (2.94 mg/ml KI corresponding to 2.25 mg/ml iodine in pure water) were placed next to the brain tissue. The verification measurement at the MuCLS revealed a concentration of 2.7 mg/ml iodine in this solution. One of the iodine-filled tubes additionally contained hydroxyapatite clusters to simulate calcification. For that, solid hydroxyapatite powder (*Sigma Aldrich, Missouri, USA*) was mixed with n-Butyl-2-Cyanoacrylat tissue glue (*Aesculap AG, Tuttlingen, Germany*) and fixed at the plastic tube walls. By that, the chemical composition of hydroxyapatite calcifications in a tissue matrix was mimicked (Mechlem *et al* 2018).

Grating interferometer setups

Attenuation coefficients, electron densities and linear diffusion coefficients are obtained with grating interferometry. The laboratory interferometers consist of a highly absorbing source grating (G0), a phase grating (G1) and a highly absorbing analyzer grating (G2) as illustrated in figure 2(a). The specifications of the interferometer components can be found in table 1.

Setup 1 (S1) uses a microfocus tube⁴ with a tungsten target, operated at an acceleration voltage of 60 kV and a power of 120 W. Images have been acquired with a Varian PaxScan 4030D flatpanel detector (*VARIAN medical systems, Palo Alto, USA*) with a structured CsI scintillator screen and a pixel size of $p = 194 \times 194 \mu\text{m}^2$. Calculation of material specific quantities requires the assignment of an effective energy to the measurements. For S1, a tungsten spectrum has been simulated (according to Siewerdsen *et al* 2004). Consideration of all absorbers in the beam path (i.e. the gratings, air and the water container) and the energy weighting of the detector, yields a mean energy of $E_\mu = 41.07$ keV. This energy is used as the effective interaction energy for the attenuation contrast. The phase and dark-field signal depend additionally on the interferometers' energy dependent visibility. Weighting of the spectrum with the energy dependent visibility $\nu(E)$ in terms of the design energy E_0

$$\nu(E) = \sin\left(\frac{\pi}{2} \cdot \frac{E_0}{E}\right)^2, \quad (1)$$

⁴ Note that x-ray source spot diameter increases to more than 100 μm for the chosen target power load, such that it is technically not a microfocus source in the described experiments (Prade 2017).

(Chabior 2011) leads to a mean energy of $E_\delta = 42.95$ keV which is used as effective interaction energy for phase and dark-field contrast.

Setup 2 (S2) is installed at a rotating molybdenum anode, which was operated at 50 kV with 1.2 kW. The used detector was a Santis photon-counting detector with a $750 \mu\text{m}$ thick cadmium telluride sensor and a pixel size of $p = 75 \times 75 \mu\text{m}^2$ (Dectris Ltd Baden-Daettwil, Switzerland). The effective interaction energies have been determined to be $E_\mu = 36.16$ keV, $E_\delta = 35.86$ keV.

As described above, the iodine concentrations have been verified at the MuCLS in a separate measurement at a two-grating interferometer (S3). The used detector was a single photon-counting Pilatus-200 K detector (Dectris Ltd Baden-Daettwil, Switzerland) with a 1 mm thick silicon sensor and a pixel size of $p = 172 \times 172 \mu\text{m}^2$. The effective interaction energy at the MuCLS was determined via a look-up table for the attenuation coefficient and the refractive index decrement of PMMA, as in Braig *et al* (2018). With an error analysis of the PMMA calibration method (mainly due to the variations of the PMMA density $\rho_{\text{PMMA}} = 1.189 \pm 0.005 \text{ g/cm}^3$), the resulting effective interaction energy for PMMA was $E_\mu = 24.7 \pm 0.2$ keV, $E_\delta = 24.4 \pm 0.2$ keV. The PMMA calibration method is feasible in case of a narrow spectral width and for measured objects with similar material properties as the calibration material. Therefore, PMMA calibration was not performed in case of the polychromatic setups but the interaction energies have been calculated from the mean of the spectra as described above⁵.

Data acquisition and processing

Three different CT measurements have been conducted at the above described interferometers. Via the so-called phase-stepping method (Pfeiffer *et al* 2006) and subsequent signal extraction with an algorithm, as published in Marschner *et al* (2016), projection images of the attenuation coefficient, the refractive index decrement gradient and the linear diffusion coefficient were obtained. This procedure was repeated for different projection angles over the range of 360° . The resulting three tomographic data sets were then reconstructed independently with a Hamming filter for the attenuation data set and the dark-field data set, and a Hilbert filter (Pfeiffer *et al* 2007) for the phase-contrast data. The measured refractive index decrement δ is related to the electron density ρ_e via

$$\delta = \frac{r_0 h^2 c^2}{2\pi E^2} \rho_e, \quad (2)$$

with the classical electron radius r_0 , the Planck constant h , the speed of light c and the energy E (Als-Nielsen *et al* 2011). As a result, the electron density is directly accessible via the measurement.

By that, the phase-stepping tomography reveals the attenuation coefficients, the electron density and the linear diffusion coefficients of the sample in 3D from a single CT acquisition and therefore with intrinsic registration of the three data sets. The attenuation coefficients were then converted to Hounsfield units (HU) and the refractive index decrement image was analogously converted to units relative to the refractive index decrement of water, which is then referred to as phase Hounsfield units (HUp), as proposed in Donath *et al* (2010). Please note that the spectra at the two laboratory setups (S1, S2) originating from a tungsten and a molybdenum tube, respectively, exhibit a different shape but result in a similar mean energy. Therefore, the HU and HUp values are not expected to be comparable between the two setups.

The respective tomography settings are given in table 2, where the measurements at setup S1, S2, S3 are referred to as M1 (iodine concentration series), M2 (brain sample) and M3 (verification of the iodine concentration series). For all measurements, the sample has been immersed into a plane parallel water container which was also in place during the reference measurements without sample to avoid spectral differences and to avoid phase shifts above 2π at strong electron density gradients. The data sets of the cylindrical iodine concentration phantom have been averaged along the cylinder axis for 30 slices. The data sets of the brain sample have been averaged by a $4 \times 4 \times 4$ pixel binning.

Effective atomic number calculation

The effective atomic number was determined as in Willner *et al* (2013), Sarapata *et al* (2015). The attenuation contrast arises mainly from three different types of photon interactions, which are the photoelectric absorption, incoherent (Compton) scattering and coherent scattering. With the so-called electronic interaction cross section $\sigma_i^e = \frac{\sigma_i}{Z}$ this can be written as

$$\mu = \rho_e \cdot (\sigma_{\text{incoh}}^e(E) + \sigma_{\text{coh}}^e(E, Z) + \sigma_{\text{ph}}^e(E, Z)) = \rho_e \cdot \sigma_{\text{tot}}^e. \quad (3)$$

⁵ Please find the spectra as supplementary material (<https://stacks.iop.org/PMB/65/185011/mmedia>).

Table 2. Measurement parameters of the three phase-contrast CT acquisitions. M1, M2, M3 are referring to the measurements at setup S1, S2, S3, respectively. The given parameters are the number of grating positions for one phase stepping, the number of projections angles, the total measurement time, the geometric magnification and the effective pixel size which accounts for the geometric magnification and the pixel binning within the tomographic slice.

Measurement	phase-steps	angles	duration [h]	magnification	$\rho_{\text{eff}}[\mu\text{m}]$
M1	7	420	7.13	1.7	115.
M2	11	1300	33.4	2.1	144.
M3	7	200	1.97	1.1	159.

With the Klein-Nishina parametrization $\mu_{\text{incoh}} = \rho_e \sigma_{\text{kn}}$, the relative contribution of Compton scattering to the linear attenuation coefficient can be given as

$$\frac{\mu_{\text{incoh}}}{\mu} = \frac{\rho_e \sigma_{\text{kn}}}{\mu} = \frac{\rho_e \sigma_{\text{kn}}}{\rho_e \sigma_{\text{tot}}^e} = \frac{\sigma_{\text{kn}}}{\sigma_{\text{tot}}/Z_{\text{eff}}}. \quad (4)$$

This gives a relation between the measured quantities μ and ρ_e and the effective atomic number

$$Z_{\text{eff}} = \frac{\rho_e}{\mu(E)} \cdot \sigma_{\text{tot}}. \quad (5)$$

This method yields the effective atomic number without empiric parametrization of the combined energy and material dependence of the photoelectric absorption and Compton scattering by interpolating the tabulated interaction cross sections as proposed in Willner *et al* (2013).

Three-material decomposition

The measured quantities μ and δ are linearly independent and can therefore be seen as basis vectors that span a two-dimensional vector space. Therefore, algebraic basis transformation can be used to display the investigated objects in terms of specific materials as known from dual-energy CT. Here, the material vectors \vec{Z}_{eff} and $\vec{\rho}_{e,\text{material}}$ were derived from the measured quantities μ and δ as described above and were used as original basis vectors and the new vector space was then chosen to be spanned by the respective iodine and water content as described previously (Braig *et al* 2018).

Additionally, the information originating from the dark-field image is used for further material discrimination. The dark-field signal is linearly independent from Z_{eff} and ρ_e , as well, and can therefore serve as a third basis vector. The dark-field signal is especially sensitive to structural fluctuations of the refractive index on a sub-resolutional length scale. Water, brain tissue and water-based iodine solutions do not exhibit such a microstructure. In contrast, calcifications, which occur in the human body in the context of various pathologies, can exhibit a microstructure. Therefore, the dark-field signal, the electron density and the effective atomic number of hydroxyapatite powder, as well as the signal of the two other basis materials iodine and water were determined at the MuCLS (S3) as reference values for three-material decomposition. Basis transformation is obtained in two steps. First, the desired basis materials (here water (W), iodine (I) and hydroxyapatite calcification (C)) are expressed as vectors in the old basis system $B = (\vec{\rho}_{e,i}, \vec{Z}_{\text{eff},i}, \vec{df}_i)$ and written as columns of the matrix

$$\mathbf{B} = \begin{pmatrix} \rho_{e,W} & Z_{\text{eff},W} & df_W \\ \rho_{e,I} & Z_{\text{eff},I} & df_I \\ \rho_{e,C} & Z_{\text{eff},C} & df_C \end{pmatrix}. \quad (6)$$

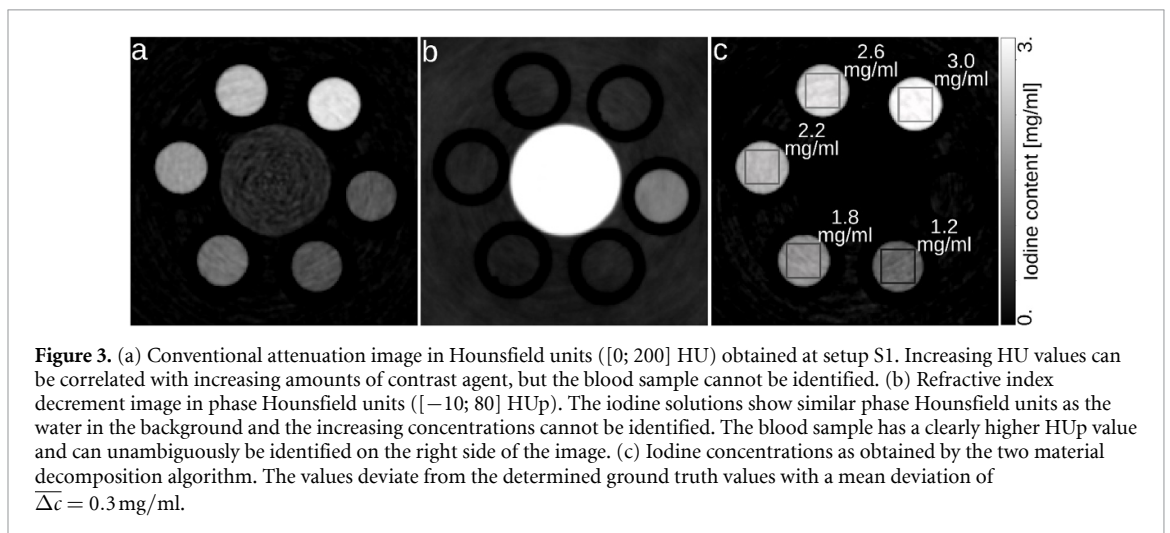
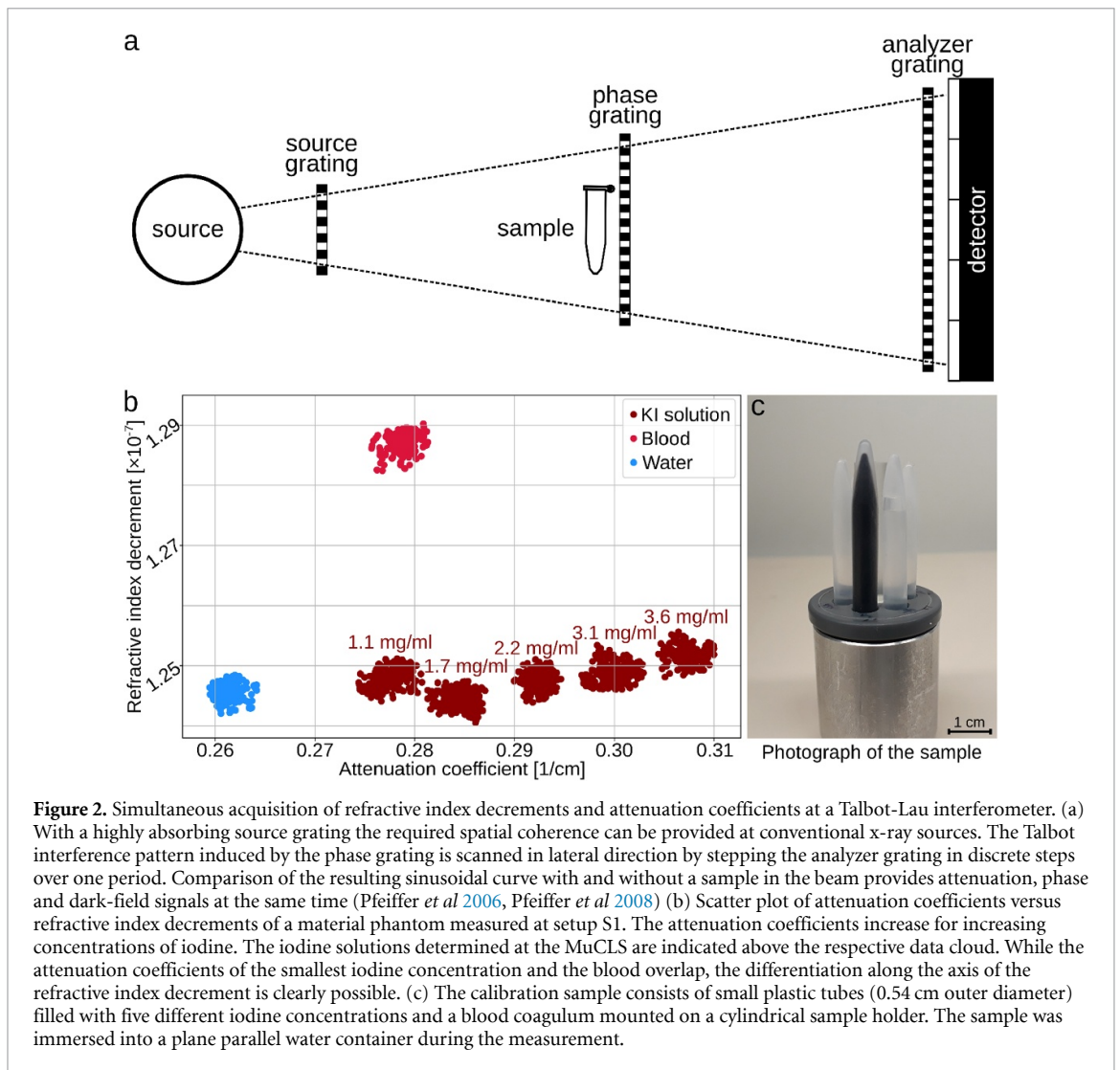
Then, the transformation matrix T must be found such that $\tilde{\mathbf{B}} = \mathbf{B}T$. The new basis system $\tilde{B}(\vec{w}, \vec{i}, \vec{c})$ which is spanned by the relative amount of the respective materials is a standard basis (\mathbf{I}) and therefore $\mathbf{B}^{-1} \cdot \mathbf{I} = \mathbf{IT}$.

For this work, the entries of the original basis system matrix \mathbf{B} were determined for the three basis materials (water, 2 mg/ml potassium iodide and hydroxyapatite powder) in a previous measurement at the quasi-monochromatic compact synchrotron source S3. The dark-field signal (df) was normalized to the maximum value measured for the hydroxyapatite powder within this calibration measurement. This determination of the quantitative basis material values must only be performed once.

3. Results

Quantitative blood iodine separation

Figure 2(a) shows a scatter plot of the attenuation coefficients and the refractive index decrements of the different materials in the material phantom (2(b)) from the measurement at setup S1. The concentrations of iodine in mg/ml are the values which have been determined in the calibration measurement at the MuCLS to



(1.1 ± 0.1) mg/ml, (1.7 ± 0.1) mg/ml, (2.2 ± 0.1) mg/ml, (3.1 ± 0.1) mg/ml and (3.6 ± 0.1) mg/ml with the statistical error derived from the standard deviation of the attenuation coefficient measurement.

While there is almost full overlap between the distributions of attenuation coefficients of the blood sample and the lowest iodine concentration, the values are clearly separated along the refractive index decrement axis. So, a separation of coagulated blood and contrast agent with the same attenuation coefficient is possible based on the refractive index decrement.

The conventional attenuation image of this sample is displayed in figure 3(a) in Hounsfield units ([0; 200] HU). The HU values of the iodine solutions increase with the iodine concentration (62.0, 88.5, 118.5, 147.9, 176.4 HU). The HU value of the blood sample is 66.6 HU and can visually not be differentiated from the lowest iodine concentration ($\text{CNR}_{\text{blood/iodine}} = 0.7$).

The refractive index element image is displayed in phase Hounsfield units ([−10; 80] HUp) in 3(b). The iodine concentrations show no visual contrast to the water in the background (1.6, −1.1, 1.4, 2.4, 4.6 HUp) but a very clear contrast to the blood sample (33.2 HUp), which can be confirmed by the CNR value of $\text{CNR}_{\text{blood/iodine}} = 19.0$.

In figure 3(c), the quantitative amount of iodine as obtained from the two-material decomposition algorithm is displayed. The mean iodine content in the marked regions (15×15 pixel) is (1.2 ± 0.1) mg/ml, (1.8 ± 0.1) mg/ml, (2.2 ± 0.1) mg/ml, (2.6 ± 0.1) mg/ml and (3.0 ± 0.1) mg/ml for the iodine-filled tubes and (0.1 ± 0.1) mg/ml for the blood-filled tube with the respective standard deviation given as a statistical error. These values vary from the previously determined ground truth values by a mean deviation of $\overline{\Delta c} = 0.3$ mg/ml. Please note, that the PMMA rod which was used for assigning the effective interaction energies at S3 was mounted on the sample holder for measurement M1 (big circle in the middle of figure 3(a) and (b)) but was not used for the analysis.

Three-material decomposition

Figure 4 shows the results of the CT of the brain sample. The conventional attenuation image (4(a)) is displayed in Hounsfield units ([0; 200] HU). The content of the three plastic tubes shows a homogeneous attenuation of 151.7 HU, 152.2 HU and 130.5 HU from left to right, respectively. The CNR value between iodine and blood is $\text{CNR}_{\text{blood/iodine}} = 0.9$ and confirms the visual impression that these materials cannot be differentiated in the conventional HU image. The brain parenchyma shows a slight contrast to the background in the way that the boundary line between the gyri and the surrounding formaldehyde solution can be seen slightly (see the white arrows in figure 4(a)). Figure 4(b) shows the refractive index decrement image displayed in HUp values ([−10; 95] HUp). From left to right, the HUp values in the plastic tubes are 4.2, 3.3, 157.8. The CNR between iodine and blood is $\text{CNR}_{\text{blood/iodine}} = 20.3$. The coagulated blood and contrast agent can be clearly differentiated visually due to the difference in their electron densities ($\rho_e(\text{blood}) = (3.86 \pm 0.02) \cdot 10^{29} \text{ m}^{-3}$, $\rho_e(\text{iodine}) = (3.35 \pm 0.01) \cdot 10^{29} \text{ m}^{-3}$). Also the brain parenchyma shows a significantly improved image contrast, such that gray and white matter can be differentiated (marked with gray arrows in figure 4(b)). In the sulci on top and on the right of the displayed slice of the sample, small regions with higher electron density can be differentiated, which could correspond to blood vessels.

The effective atomic number is displayed in pseudo colors (4(c)) as in clinical dual-energy CT scanners. The iodine content image (4(d)) shows the quantitative amount of iodine from the three-material decomposition algorithm in the plastic tubes, which are from left to right (2.2 ± 0.3) mg/ml, (2.2 ± 0.2) mg/ml, (0.0 ± 0.0) mg/ml.

Figure 4(e) shows the dark-field signal strength in terms of the third basis material (hydroxyapatite). The third basis vector is used for the extraction of the small-angle scattering power of a material. The dark-field image typically shows an enhanced signal at sub-resolutional electron-density fluctuations as can be seen at the borders of the blood-filled tube or in general at the interfaces between the plastic tubes and the surrounding fluid. Besides, there is a brighter spot at the border of the plastic tube in the middle (as marked by the light gray arrow in figure 4(e)). A closer look at the conventional HU image and the HUp image reveals a signal at the same position that is smaller in its dimensions. The feature is not present in the iodine content image and can be unambiguously identified as the hydroxyapatite deposition, which had been fixed at the tube wall prior to the experiment. Within the blood sample, a further dark-field feature can be seen that has no equivalent signal in the attenuation image. In a different HUp window, this feature can also be seen in the phase-contrast image. As the tube contains only the coagulated blood, it is assumed that the signal corresponds to a very dense agglomeration of blood cells during the coagulation process.

A direct comparison of two- and three-material decomposition from the same measurement is presented in figure 5. When decomposing the original image into the water and iodine content based on the attenuation and phase signal alone, the hydroxyapatite cluster falsely appears in the iodine content image (figure 5(a), white arrows). Additional consideration of the dark-field signal, allows a clear identification and separation of the hydroxyapatite cluster which is not present in the iodine content image after three-material decomposition (figure 5(b), white arrows). Both, two- and three-material decomposition allow the clear separation of iodine contrast agent and the blood coagulum with a slightly lower iodine value in the upper plastic tube in three-material decomposition.

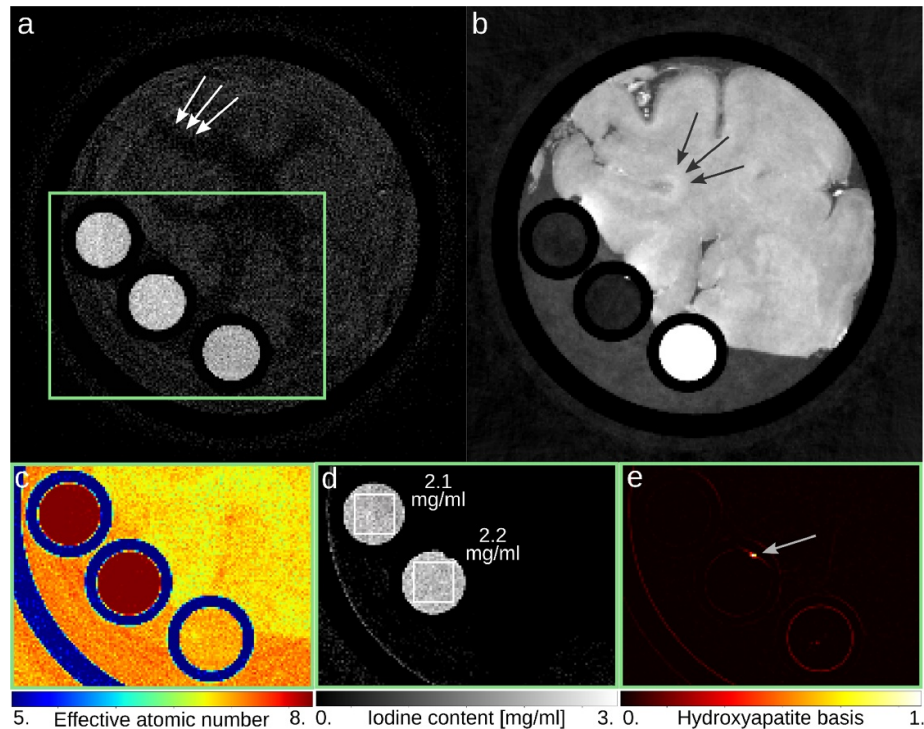


Figure 4. Multi-modal representation of a part of a pig brain (frontal lobe) based on a single CT acquisition at setup S2. (a) Besides the conventional attenuation image, which is displayed in Hounsfield units ($[0; 200]$ HU), further image representations are available for diagnosis. (b) In the electron density image (displayed in phase Hounsfield units ($[-10; 95]$ HUp)), the clotted blood can clearly be identified and differentiated from the contrast agent. (c) The effective atomic number image is displayed in pseudo colors as known from dual-energy CT. (d) The iodine content can be determined quantitatively by three-material decomposition. (e) The dark-field image is displayed in terms of the normalized hydroxyapatite basis vector and it reveals a calcification within the iodine-filled tube (light gray arrow), which does not occur in the iodine content image. The brain sample was positioned in a plastic tube with 2.9 cm outer diameter. The iodine solutions and the blood coagulum were filled into small plastic tubes with 0.54 cm outer diameter.

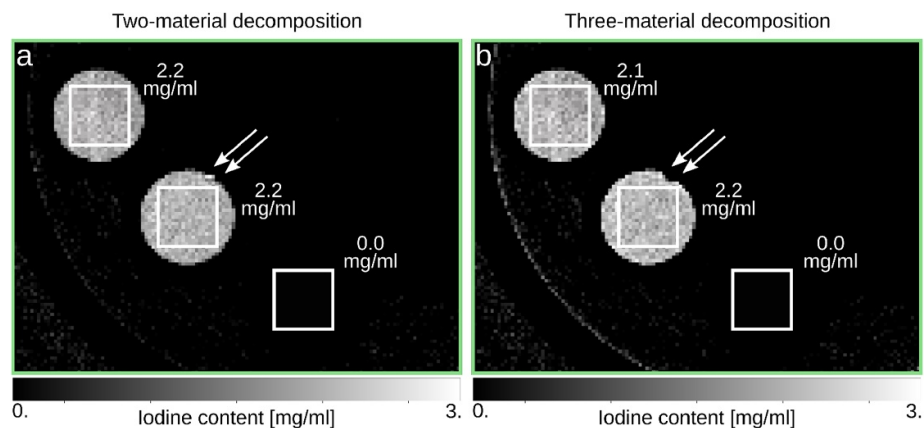


Figure 5. Comparison of material separation in two- and three-material decomposition. (a) The iodine content image reveals the quantitative amount of iodine in the two plastic tubes and allows a clear separation of contrast agent and the blood coagulum. The separation of contrast agent and the calcification is not possible by two-material decomposition, as the hydroxyapatite cluster is present in the iodine content image (marked by the white arrows). (b) Three material decomposition based on the attenuation, phase and dark-field signals, allows the clear separation of contrast agent, the blood coagulum and the hydroxyapatite cluster. The calcification (white arrows) and the blood coagulum (lowest white box) are separated from the iodine content image. The outer green box marks the respective enlarged region in figure 4(a).

4. Discussion

This study demonstrates that quantitative material decomposition is possible at conventional polychromatic x-ray sources with Talbot-Lau interferometers and with higher x-ray energies compared to previous experiments (Braig *et al* 2018). It has been shown how the additional information on the electron density

and the microstructure of a material can be used to discriminate materials that are relevant in stroke diagnosis based on a single CT acquisition.

With a simple material decomposition algorithm, the amount of iodine in a calibration phantom has been determined. With a mean deviation of 0.3 mg/ml, the precision of the determination of the absolute amount of iodine in this small soft tissue sample is similar to commercially available dual-energy CT devices (Pelgrim *et al* 2017, Koonce *et al* 2014, Sellerer *et al* 2018), while the relative deviation for the smallest concentrations is up to 17% compared to the ground truth values determined at the MuCLS. Comparison with the original nominal solutions reveals a smaller mean deviation of 0.2 mg/ml. As the ground truth concentrations are systematically higher than the nominal concentrations that were prepared, it cannot be excluded that the concentrations have increased due to evaporation between the measurements. However, it has been seen in a previous study that the hygroscopic effect of iodine, leads to a systematic overestimation of the nominal concentrations (Braig *et al* 2018). Therefore, the precision of the iodine quantification could be better than stated above, which should be analyzed with a well-defined iodine calibration phantom in the future.

A post-interventional stroke scenario with unclear diagnosis has been experimentally simulated with a brain sample, a blood coagulum, contrast agent and a small calcification. While blood and contrast agent cannot be discriminated in the conventional attenuation image, the additional electron density based image allows for a clear identification of the two materials. Further, three-material decomposition has been performed, such that the quantitative amount of iodine and the presence of hydroxyapatite clusters can be analyzed in separate basis images, which simplifies and clarifies diagnosis. The proposed method allows for discrimination of the involved materials based on a single CT acquisition. This implies a potential concept for simplifying post-interventional stroke diagnosis which is up to now in clinical routine based on several follow-up investigations.

While the approach of grating-based material decomposition has successfully been transferred from a quasi-monochromatic x-ray source with a mean energy of ≈ 25 keV to polychromatic x-ray sources with mean energies of up to 43 keV, further steps are necessary to achieve clinical feasibility. In principle, the technical feasibility to mount the interferometer on a rotating CT gantry (Tapfer *et al* 2012), the decrease of the scanning time by the use of advanced acquisition schemes (Marschner *et al* 2016, von Teuffenbach *et al* 2017), the reduction of the radiographic dose level to clinically approved values (Willer *et al* 2018, Gromann *et al* 2017, Fingerle *et al* 2019), *in vivo* imaging for small animals as well as for pigs (Bech *et al* 2013, Hellbach *et al* 2015, Yaroshenko *et al* 2015, Gromann *et al* 2017) and the increase of the x-ray energy and the field of view for applications suitable for the human chest (Willer *et al* 2018, Gromann *et al* 2017, Fingerle *et al* 2019, De Marco *et al* 2019) have been successfully demonstrated within the last years. However, the combined fulfillment of all these requirements to enable clinical grating-based CT imaging remains an ambitious task. Apart from these technical challenges, the increase of the x-ray energy limits the complementarity of the attenuation and the phase-contrast image due to the decreasing contribution of photoelectric absorption to the x-ray attenuation. As the interaction cross section for photoelectric absorption scales with the atomic number of the material ($\sigma_{ph}(Z) \propto Z^k$, with $k \approx 4 - 5$ (White 1997, Contillo and Taibi 2017)), the material decomposition cannot be expected to work for soft tissue material like brain parenchyma at a diagnostic x-ray energy for head CT. But the complementarity remains longer for higher atomic number materials like iodine contrast agent and calcifications. The high diagnostic relevance of these materials preserves the benefits of decomposition approaches at higher energies as exploited for clinical dual-energy CT.

On the other hand, the phase sensitivity that defines the smallest resolvable electron density difference will be substantially decreased for first interferometer designs suitable for humans (Chabior 2011). The phase sensitivity scales with a function of the period of the analyzer grating p_2 , the inter-grating distance d and the standard deviation of the photon statistics σ_ϕ such that the smallest resolvable refraction angle is $\alpha_{\min} = \sigma_\phi \cdot p_2 / 2\pi d$. In the presented experiment, the electron density difference between blood and contrast agent ($\Delta\rho_e > 0.335 \cdot 10^{29} \text{m}^{-3}$) was more than 22 times higher than the standard deviation in the electron density images $\sigma < 0.015 \cdot 10^{29} \text{m}^{-3}$ so that the discrimination would still be possible with moderately decreased phase sensitivity.

Unlike the attenuation coefficient and the electron density, the quantitative interpretation of the dark-field signal is still under discussion (Malecki *et al* 2012, Strobl 2014, Wolf *et al* 2015). It is possible to define a linear diffusion coefficient in analogy to the linear attenuation coefficient, which expresses the dark-field signal independent from the interferometer design (Bechet *et al* 2010). However, the dark-field signal strength is dependent on the sub-micrometer structure of a material and is not an intrinsic chemical property in the same sense as the electron density or the atomic number. Therefore, the third basis vector is used for the extraction of the quantitative small-angle scattering power of a material as a novel type of material specification. This can be an advantage in the diagnosis of all pathologies that involve microcalcifications or any type of strong refractive index fluctuations on a sub-resolution length scale

(e.g. structural changes of the lung alveoli (Bech *et al* 2013) or urate deposition (Scherer *et al* 2015) among others). As the signal also arises at material borders, strong electron density fluctuations or from strongly absorbing materials, radiologists must be trained on the interpretation of this novel signal and especially on drawing conclusions from correlations between the different image channels.

5. Conclusion

It was demonstrated how the threefold imaging data from grating-based phase-contrast CT can be used for three-material decomposition. It was possible to determine iodine concentrations quantitatively, to identify and visualize a blood coagulation in an electron-density based image and to separate small hydroxyapatite clusters via the small angle scattering signal within a single CT acquisition. The method has been proven compatible with conventional x-ray sources as used in clinical imaging without specific requirements for the x-ray detector. While the technical realization of a clinical Talbot-Lau CT system is still under development, x-ray dark-field and phase-contrast imaging is already available in radiographic systems approved for first patient studies (Tanaka *et al* 2013, Arboleda *et al* 2019). With the here presented method for three-material decomposition, we would like to propose an additional feature of gbpc-CT as a basis for further technical development. Besides the simultaneous acquisition of all image signals and therefore perfect spatial and temporal registration, the biggest advantage of the method is the additional dark-field information, which is not accessible with any other clinical imaging method until now.

Acknowledgments

We acknowledge the support through the European Research Council (AdG 695045). The Munich Compact Light Source is supported through the Center for Advanced Laser Applications (CALA). This work was carried out with the support of the Karlsruhe Nano Micro Facility (KNMF, www.kit.edu/knmf), a Helmholtz Research Infrastructure at Karlsruhe Institute of Technology (KIT). The authors thank the staff of Lyncean Technologies Inc. for their technical support at the MuCLS and also thank the Research Training Group GRK2274.

ORCID iDs

Eva-Maria Braig  <https://orcid.org/0000-0002-7275-0447>

Martin Dierolf  <https://orcid.org/0000-0001-5150-2949>

References

- Als-Nielsen J and Des M 2011 *Elements of Modern X-ray Physics* (Chichester: John Wiley) (<http://site.ebrary.com/lib/alltitles/docDetail.action?docID=10510633>)
- Arboleda C *et al* 2019 Towards clinical grating-interferometry mammography *Eur. Radiol.* **30** 1419–25
- Bech M, Bunk O, Donath T, Feidenhans R, David C and Pfeiffer F 2010 Quantitative x-ray dark-field computed tomography *Phys. Med. Biol.* **55** 5529
- Bech M, Tapfer A, Velroyen A, Yaroshenko A, Pauwels B, Hostens J, Bruyndonckx P, Sasov A and Pfeiffer F 2013 In-vivo dark-field and phase-contrast x-ray imaging *Sci. Rep.* **3** 3209
- Birnbacher L *et al* 2016 Experimental realisation of high-sensitivity laboratory x-ray grating-based phase-contrast computed tomography *Sci. Rep.* **6** 24022
- Birnbacher L, Willner M, Marschner M, Pfeiffer D, Pfeiffer F and Herzen J 2018 Accurate effective atomic number determination with polychromatic grating-based phase-contrast computed tomography *Opt. Express* **26** 15153–66
- Braig E *et al* 2018 Direct quantitative material decomposition employing grating-based x-ray phase-contrast CT *Sci. Rep.* **8** 16394
- Chabior M 2011 Contributions to the characterization of grating-based x-ray phase-contrast imaging *PhD Thesis* Technical University of Munich
- Contillo A and Taibi A 2017 Material characterisation in phase contrast imaging: The basis decomposition method revisited *EPL (Europhys. Lett.)* **117** 48003
- De Marco F *et al* 2019 Contrast-to-noise ratios and thickness-normalized, ventilation-dependent signal levels in dark-field and conventional in vivo thorax radiographs of two pigs *PloS One* **14** e0217858
- Djurdjevic T, Rehwald R, Knoflach M, Matosevic B, Kiechl S, Gizewski E R, Glodny B and Grams A E 2017 Prediction of infarction development after endovascular stroke therapy with dual-energy computed tomography *Eur. Radiol.* **27** 907–17
- Donath T, Pfeiffer F, Bunk O, Grünzweig C, Hempel E, Popescu S, Vock P and David C 2010 Toward clinical x-ray phase-contrast CT: demonstration of enhanced soft-tissue contrast in human specimen *Investigative Radiol.* **45** 445–52
- Fingerle A A *et al* 2019 Imaging features in post-mortem x-ray dark-field chest radiographs and correlation with conventional x-ray and CT *Eur. Radiol. Experimental* **3** 25
- Graser A, Johnson T R, Chandarana H and Macari M 2009 Dual energy CT: preliminary observations and potential clinical applications in the abdomen *Eur. Rad.* **19** 13
- Gromann L B *et al* 2017 In-vivo x-ray dark-field chest radiography of a pig *Sci. Rep.* **7** 4807
- Gupta R, Phan C M, Leidecker C, Brady T J, Hirsch J A, Nogueira R G and Yoo A J 2010 Evaluation of dual-energy CT for differentiating intracerebral hemorrhage from iodinated contrast material staining *Radiology* **257** 205–11

- Hellbach K *et al* 2015 In vivo dark-field radiography for early diagnosis and staging of pulmonary emphysema *Investigative Radiol.* **50** 430–5
- Herzen J, Donath T, Pfeiffer F, Bunk O, Padeste C, Beckmann F, Schreyer A and David C 2009 Quantitative phase-contrast tomography of a liquid phantom using a conventional x-ray tube source *Opt. Express* **17** 10010–18
- Jacobsen M C, Schellingerhout D, Wood C A, Tamm E P, Godoy M C, Sun J and Cody D D 2018 Intermanufacturer comparison of dual-energy CT iodine quantification and monochromatic attenuation: a phantom study *Radiology* **287** 224–34
- Johnson T R *et al* 2007 Material differentiation by dual energy CT: initial experience *European Radiology* **17** 1510–17
- Kane I, Whiteley W, Sandercock P and Wardlaw J 2008 Availability of CT and MR for assessing patients with acute stroke *Cerebrovascular Diseases* **25** 375–7
- Kim Y, Kim Y K, Lee B E, Lee S J, Ryu Y J, Lee J H and Chang J H 2015 Ultra-low-dose CT of the thorax using iterative reconstruction: evaluation of image quality and radiation dose reduction *Am. J. Roentgenol.* **204** 1197–202
- Koonce J D, Vliegthart R, Schoepf U J, Schmidt B, Wahlquist A E, Nietert P J, Bastarrika G, Flohr T G and Meinel F G 2014 Accuracy of dual-energy computed tomography for the measurement of iodine concentration using cardiac CT protocols: validation in a phantom model *Eur. Radiol.* **24** 512–18
- Korn A *et al* 2012 Iterative reconstruction in head CT: image quality of routine and low-dose protocols in comparison with standard filtered back-projection *Am. J. Neuroradiol.* **33** 218–24
- Larson D B, Johnson L W, Schnell B M, Salisbury S R and Forman H P 2011 National trends in CT use in the emergency department: 1995–2007 *Radiology* **258** 164–73
- Malecki A, Potdevin G and Pfeiffer F 2012 Quantitative wave-optical numerical analysis of the dark-field signal in grating-based x-ray interferometry *EPL (Europhys. Lett.)* **99** 48001
- Marschner M, Willner M, Potdevin G, Fehringer A, Noël P, Pfeiffer F and Herzen J 2016 Helical x-ray phase-contrast computed tomography without phase stepping *Sci. Rep.* **6** 23953
- McCullough C H, Leng S, Yu L and Fletcher J G 2015 Dual- and multi-energy CT: principles, technical approaches, and clinical applications *Radiology* **276** 637–53
- Mechlem K, Sellerer T, Ehn S, Münzel D, Braig E, Herzen J, Noël P B and Pfeiffer F 2018 Spectral angiography material decomposition using an empirical forward model and a dictionary-based regularization *IEEE Trans. Med. Imaging* **37** 2298–309
- Michel T *et al* 2013 On a dark-field signal generated by micrometer-sized calcifications in phase-contrast mammography *Phys. Med. Biol.* **58** 2713
- Miglioretto D L *et al* 2013 The use of computed tomography in pediatrics and the associated radiation exposure and estimated cancer risk *JAMA Pediatrics* **167** 700–7
- Mokin M, Kan P, Kass-Hout T, Abla A A, Dumont T M, Snyder K V, Hopkins L N, Siddiqui A H and Levy E I 2012 Intracerebral hemorrhage secondary to intravenous and endovascular intraarterial revascularization therapies in acute ischemic stroke: an update on risk factors, predictors, and management *Neurosurgical Focus* **32** E2
- Payabvash S, Qureshi M H, Khan S M, Khan M, Majidi S, Pawar S and Qureshi A I 2014 Differentiating intraparenchymal hemorrhage from contrast extravasation on post-procedural noncontrast CT scan in acute ischemic stroke patients undergoing endovascular treatment *Neuroradiology* **56** 737–44
- Pelgrim G J *et al* 2017 Accuracy of iodine quantification using dual energy CT in latest generation dual source and dual layer CT *Eur. Radiol.* **27** 3904–12
- Pfeiffer F, Bech M, Bunk O, Kraft P, Eikenberry E F, Brönnimann C, Grünzweig C and David C 2008 Hard-x-ray dark-field imaging using a grating interferometer *Nat. Mater.* **7** 134
- Pfeiffer F, Bunk O, Kottler C and David C 2007 Phase retrieval and differential phase-contrast imaging with low-brilliance x-ray sources *Nucl. Instrum. Methods Phys. Res. A* **580** 925–8
- Pfeiffer F, Weitkamp T, Bunk O and David C 2006 Phase retrieval and differential phase-contrast imaging with low-brilliance x-ray sources *Nat. Phys.* **2** 258–61
- Phan C, Yoo A, Hirsch J, Nogueira R and Gupta R 2012 Differentiation of hemorrhage from iodinated contrast in different intracranial compartments using dual-energy head CT *Am. J. Neuroradiol.* **33** 1088–94
- Postma A A, Hofman P A, Stadler A A, van Oostenbrugge R J, Tijssen M P and Wildberger J E 2012 Dual-energy CT of the brain and intracranial vessels *Am. J. Roentgenol.* **199** S26–S33
- Potdevin G *et al* 2012 X-ray vector radiography for bone micro-architecture diagnostics *Phys. Med. Biol.* **57** 3451
- Prade F 2017 Grating-based x-ray dark-field imaging - theory and applications in materials research *PhD Thesis* Technical University of Munich
- Qi Z, Zambelli J, Bevins N and Chen G H 2010 Quantitative imaging of electron density and effective atomic number using phase contrast CT *Phys. Med. Biol.* **55** 2669
- Sarapata A *et al* 2015 Quantitative imaging using high-energy x-ray phase-contrast CT with a 70 kVp polychromatic x-ray spectrum *Opt. Express* **23** 523–35
- Scherer K *et al* 2015 Non-invasive differentiation of kidney stone types using x-ray dark-field radiography *Sci. Rep.* **5** 9527
- Scherer K *et al* 2016 Improved diagnostics by assessing the micromorphology of breast calcifications via x-ray dark-field radiography *Sci. Rep.* **6** 36991
- Schleede S *et al* 2012 Emphysema diagnosis using x-ray dark-field imaging at a laser-driven compact synchrotron light source *Proc. Natl. Acad. Sci.* **109** 17880–5
- Sellerer T *et al* 2018 Dual-energy CT: a phantom comparison of different platforms for abdominal imaging *European Radiology* **28** 2745–55
- Siewerdsen J, Waese A, Moseley D, Richard S and Jaffray D 2004 Spektr: a computational tool for x-ray spectral analysis and imaging system optimization *Med. Phys.* **31** 3057–67
- Strobl M 2014 General solution for quantitative dark-field contrast imaging with grating interferometers *Sci. Rep.* **4** 7243
- Tanaka J, Nagashima M, Kido K, Hoshino Y, Kiyohara J, Makifuchi C, Nishino S, Nagatsuka S and Momose A 2013 Cadaveric and in vivo human joint imaging based on differential phase contrast by x-ray Talbot-Lau interferometry *Z. Med. Physik* **23** 222–7
- Tapfer A *et al* 2012 Experimental results from a preclinical x-ray phase-contrast CT scanner *Proc. Natl Acad. Sci.* **109** 15691–6
- Tijssen M, Hofman P, Stadler A, Van Zwam W, De Graaf R, Van Oostenbrugge R, Klotz E, Wildberger J and Postma A 2014 The role of dual energy CT in differentiating between brain haemorrhage and contrast medium after mechanical revascularisation in acute ischaemic stroke *Eur. Radiol.* **24** 834–40
- Webb W R, Brant W E and Major N M 2019 *Fundamentals of Body CT E-Book* (Amsterdam: Elsevier)

- Wen H, Bennett E E, Hegedus M M and Rapacchi S 2009 Fourier x-ray scattering radiography yields bone structural information *Radiology* **251** 910–18
- White D 1977 An analysis of the Z-dependence of photon and electron interactions *Phys. Med. Biol.* **22** 219
- Willer K *et al* 2018 x-ray dark-field imaging of the human lung—A feasibility study on a deceased body *PloS One* **13** e0204565
- Willner M *et al* 2013 Quantitative x-ray phase-contrast computed tomography at 82 keV *Opt. Express* **21** 4155–66
- Wolf J, Sperl J I, Schaff F, Schüttler M, Yaroshenko A, Zanette I, Herzen J and Pfeiffer F 2015 Lens-term- and edge-effect in x-ray grating interferometry *Biomed. Opt. Express* **6** 4812–24
- Yaroshenko A *et al* 2015 Improved in vivo assessment of pulmonary fibrosis in mice using x-ray dark-field radiography *Sci. Rep.* **5** 17492
- von Teuffenbach M *et al* 2017 Grating-based phase-contrast and dark-field computed tomography: a single-shot method *Sci. Rep.* **7** 7476